Effects of Nanometer Particle Size on the Properties of Activated Carbon from Terminalia Catappa Fruits Waste

Noorain Purhanudin
Fadzidah Mohd Idris (fadzidahmohdidris@usim.edu.my)
Universiti Sains Islam Malaysia
Nur Fadilah Baharuddin Pallan

Research Article

Keywords: activated carbon, Terminalia catappa, particle size, nanoscale, mesopores

Posted Date: November 14th, 2022

DOI: https://doi.org/10.21203/rs.3.rs-2239940/v1

Abstract

Activated carbon (AC) derived from agricultural by-products, such as *Terminalia catappa* (TC) fruit waste has been demonstrated as a potential AC material in reducing the production cost in the industry. It also retains the benefits of agricultural by-products, such as being abundant and renewable, environmentally safe, and structurally porous. Several studies have been conducted on the materials' properties of the prepared ACs from TC fruits at various particle sizes. The top-down approach of high energy ball milling (HEBM) is a simple technique used in reducing the particle size of TC to the nanoscale. Moreover, the ACs have been successfully synthesized by pre-carbonization methods, as well as chemical and physical activations. The pre-carbonization process was performed at 400 ^{o}C for 4 hours. The chemical activation was conducted using the KOH impregnation ratio as an activating agent, and a further physical process to activate the carbon was performed in a horizontal tube furnace at 750 ^{o}C for two hours with N_2 gas flow. The properties and characteristics of *Terminalia catappa* fruits as ACs were obtained by calculating the percentage yield of ACs and analysis of the surface morphology and elemental composition, particle size, phase analysis, structural analysis, and surface area by using FESEM-EDX, TEM, XRD, Raman spectroscopy, and BET respectively. The percentage yield of ACs was increased with reduced particle size from TC powder, which was in the range of 30–71%. The surface morphology of the prepared ACs reflected the porous structure and the most abundant elements found in the ACs

were C, O, and K. The average particle size of all crushed samples obtained was less than 100 nm. The XRD result confirmed the formation of crystalline structures of the graphitic carbon. The results of surface area analysis indicate that the pore size of the activated carbon is mostly in the range of mesopore, whereas the structural analysis depicts that the ratio of I_D/I_G of AC is nearly the same in between 0.8 to 0.92 and is slightly lower than TC. Thus, the development of agricultural waste-derived mesoporous activated carbon materials is potentially useful for various applications.

Introduction

Global issues, particularly environmental pollution and energy constraints have increased the need for eco-sustainable materials. Activated carbon (AC), as one of the carbonaceous materials family, is seen as a potential candidate due to its high absorption of organic molecules and metal ions from the environment, making it cost-effective and environmentally benign [1, 2]. The AC possesses rapid adsorption capacity [3], low acid-base reactivity, and good thermal stability [4]. The rate and amount of the adsorption depend on the carbon characteristics and the experimental design [5]. The potential application of ACs in a wide range of fields, such as air and gas purification and wastewater treatment [9], is linked to its exceptional properties controllable pore structure, high micropore volume and tunable surface-containing functional groups [6–8]. According to Roozbeh et al. (2013), the carbonaceous material is carbonized at a high temperature in a furnace under an inert condition and subsequently activated by using oxidizing gases, such as carbon dioxide (CO_2), steam, air, or a combination of them to produce char with the desired porosity corresponding to the physical activation method [5]. The factors for activation correspond to the properties of the precursor, chemical substances, particle size, retention time, impregnation ratio, procedure configuration, and activation period [10]. New pores and the widening of narrow pores developed on the surface of char during the physical activation enhanced the carbonaceous structure porosity and surface area [11].

AC can be prepared basically by two methods: one-step method and two-step method both involving physical and chemical activations. However, the quality of AC and percentage yield of carbon is relatively lower for physical activation compared to chemical activation. This is consistent with the high quality of AC attributed to higher activation temperature and the prolonged activation process [10]. In a one-step method, the agricultural by-product precursor is impregnated with a chemical activator, followed by activation to produce an agricultural-derived AC. Meanwhile, the two-step method involves pre-

carbonizations and an activation process. During the pre-carbonization process, the agricultural by-products are thermally converted into char. AC obtained from the one-step method has poor texture characteristics, such as lower specific surface area and smaller porosity due to the lack of a carbonization process to optimize the microstructure of the carbon matrix. However, this step shortens the preparation process and reduces energy consumption [12]. Generally, the activation process involved in the AC preparations functions as a key in synthesizing AC with the adsorption capabilities, formation of pore structure, and distribution [13]. According to Fu et al. (2019), the results obtained from the two-step method can produce a superior yield of AC with a higher specific surface area and larger pore volume than the one-step method [14]. Moreover, chemical activation results in higher percentage yield, better-developed pore structure, and larger surface areas since it requires lower operating and energy costs as lower temperatures are used compared to physical activation [15–17].

The raw materials and preparation methods used in synthesizing AC considerably affect the properties, quality, and cost. Commercial AC is derived from fossil fuel-based materials such as coal, peat, and lignite [18]. Due to environmental and health awareness, those materials are said to be toxic and corrosive, which may affect the performance of the AC with the presence of impurities [19]. AC can be produced, theoretically, from any carbonaceous material rich in carbon elements. Researchers have recently focused on the production of activated carbon from agricultural by-products and residual wastes due to the high cost of traditional coal-based AC. Numerous studies have demonstrated the wide application of AC from agricultural waste in reducing production costs and as an effective approach in resolving disposal management based on its high specific surface area due attributed to high volatile matter, lignocellulosic content, and renewable resource function [20–22]. Shuang Wanga et al., (2020) reported that this waste is a renewable resource that can be better managed and utilized in various fields [23, 24].

In the process of preparing the source materials, high energy ball milling (HEBM) is the most useful technology that can be employed as a tool for reducing the particle size of a material [25, 26]. The technique was found applicable for surface modification of agricultural waste materials, which enhanced the exposed surface areas and functionality without altering their intrinsic properties [27]. HEBM process consists of powders that are exposed to the repeated action of hitting balls, and the energy is transferred from the balls to the trapped powder during their hits, thereby promoting different phenomena. Generally, the milling process is a crushing process usually applied in the materials science research field in reducing the particle dimensions by crushing the original grains into smaller ones. The synthesized products have unique characteristics that are often not achievable by using other techniques. HEBM was used to synthesize metal powders mechanically, which led to both amorphous and nanocrystalline intermetallic compounds. Benjamin et al. (1970) reported the first application of HEBM with higher revolutions per minute (r.p.m) to synthesize new oxide dispersion-strengthened alloys [28], which is universally applicable for quick drying or wet grinding of organic and inorganic samples [29, 30].

This study aims to explore the feasibility of preparing high-quality AC from *Terminalia catappa* (TC) fruit shell waste at various particle sizes undergoing different milling times using the HEBM technique. The

conversion of raw materials into high-quality AC was carried out by using a combination of heating carriers in a tube furnace and chemical activation with potassium hydroxide (KOH) as an activating agent. The agricultural waste is converted into ash since the furnace accommodates only a small quantity of material [9]. Hence, the tube furnace is fabricated in such a way that the materials are introduced into the horizontal furnace and burned in a nitrogen flow as an inert atmosphere and converted into activated carbon [31–34]. The feasibility of using carbon adsorbents based on TC has also been studied. The characterization of activated carbons was performed using X-ray diffraction, field emission scanning electron microscope, Raman spectroscopy, transmission electron microscope and N_2 adsorption-desorption isotherms.

Materials And Methodology

Materials

Terminalia catappa (TC) fruit waste was collected from the Malaysian East Coast region as the natural resource for this research. The TC fruits were gathered, cleaned, and exposed to the scorching sun for two days before being oven-dried overnight at 110 ^{o}C. The external coatings of the TC fruits were peeled, cleaned, and ground into a coarse size using a high-energy crusher (sample assigned as TC crush), and the husk was removed. The grinding process was carried out for 15 minutes until the powder form was obtained. The grain size was later sieved using a sieve plate of size 25 µm. The milling process of the TC powder was subsequently performed in a SPEX SamplePrep 8000D Mixer/Mill® mill together with tungsten carbide balls (WC) in a 1:10 ratio using a high-energy ball milling (HEBM) technique. The process was carried out at speeds of 1200 revolutions per minute (r.p.m) for 10, 12, and 14 hours to obtain a homogeneous TC powder with three different average particle sizes predicted in nanometers. The samples of TC powder were labeled as TC0, TC10, TC12, and TC14 in accordance with the milling time.

Preparation of Activated Carbon

All the TC powder was pre-carbonized in a horizontal tube furnace at 400°C for four hours. The pre-carbonized TC powder was chemically activated for 24 hours and conducted at room temperature using KOH as the activating agent. The pre-carbonized TC powder was impregnated with a 1:5 impregnation ratio in a 50% potassium hydroxide (KOH) solution. The slurry was allowed to dry after being stirred with a magnetic stirrer. After being ground into a powder with a pestle and mortar, the samples were physically activated for the carbonization process. The samples were physically activated in a tube furnace with a nitrogen flow rate of 5 sccm and a temperature of 750°C, which was maintained for two hours. Consequently, the activated carbon (AC) was washed with distilled water repeatedly to remove residual organics and neutralize the washing solution until the pH reaches 7. The samples were filtered and dehydrated in an oven at 110°C for 12 hours. Activated carbon with a milling time of 10, 12, and 14 hours was labeled as AC10, AC12, and AC14, respectively. The percentage yield of activated carbon was estimated according to Eq. (1) [35–37]:

$$yield\,(\%) = \frac{m_f}{m_0} \times 100\%$$

1

where m_f and m_0 are the mass of activated carbon and the mass of the sample before activation, respectively.

Characterization of the physical properties of activated carbon

The characterization of the sample involved the physical and chemical properties of activated carbon, including the yield, surface morphology, element, microstructure, surface area, and chemical bonding. The morphological surface and element composition were examined through field emission scanning electron microscope (FESEM) images and energy dispersive X-ray (EDX) with liquid nitrogen. The samples were covered in a conductive platinum coating before the surface analysis. X-ray diffraction (XRD) was utilized to examine the structural alterations in the AC crystals by using an X-ray diffractometer (Rigaku Miniflex 600). Raman spectroscopy was used to determine the structure of the carbon framework of the prepared activated carbon materials. The Raman spectra of activated carbon materials have been investigated by a peak-deconvolution technique to obtain the structural characteristics. Studies of the surface area of the prepared ACs utilized the Brunauer-Emmett-Teller (BET) method. We also reported an attempt to extract the pore structure of activated carbon from transmission electron microscopy (TEM) images.

Results And Discussion

Particle Size Analysis (TEM)

Figure 1 displays the TEM micrograph and particle size distribution of samples TC A0 and TC C12. The average particle sizes of TC A0 and TC C12 are 61.5 nm and 51.8 nm, respectively. The particle size distribution for sample TC A0 depicts a broad range of distribution between 30 to 150 nm. As for sample TC C12, the particle size distribution ranges from 20 to 100 nm, indicating that the particle size distribution approaches lower diameter size as the starting particle size decreases due to the milling process. As for sample TC D14, the average particle size did not reflect a significant improvement since the difference in the starting particle size milling time was only two hours. Moreover, exceeding the milling time beyond a critical value may result in some drawbacks [38].

The ball milling technique led to a maximum rupture of particles during the initial hours, and it remained a minimum for a long time. This result corroborates the findings of several researchers [39–41]. Due to both the uniform movement of balls and attrition during ball milling, particle sizes after 12 hours (51 nm) are likely to be reduced compared to the TC crush without milling. The results are consistent with those of Abdullah and Wu (2009) and Akos et al. (2005) [42–43].

Percentage Yield of Activated Carbon Analysis

Figure 2 displays the percentage yield of activated carbon for different milling times TC to synthesize AC. The yield of activated carbons (ACs) increased from 28.85–71.62% as the milling time increased from 10 hours to 14 hours, respectively. These results indicate that different milling times as starting particle size influenced the yield of activated carbon. This finding aligns with the report by García et al. (2019) in which the milling process improved all properties by 40 to 70% [44]. The percentage yield of activated carbon for AC A0 crush, AC B10, AC C12, and AC D14 was 50.52%, 31.73%, 39.43%, and 71.62% respectively.

Phase Analysis (XRD)

The crystalline structures of milled and activated carbon prepared from *Terminalia catappa* were determined by using an X-ray diffractometer. The samples are scanned with 2θ angles from 10^0 to 90^0. Figure 3 presents the XRD pattern of TC at different milling times (TC B10, TC C12, TC D14) and the crystalline phase of AC (AC A0, AC B10, AC C12, AC D14) was identified. TC powder depicts the presence of the amorphous structure based on broad peaks detected at diffraction peaks 2θ around 21^0 and 43.6^0 exhibiting characteristics of carbon peaks of (002) and (100) planes, respectively [45]. The broad peak with a hump confirms the presence of porous and amorphous structures with a low degree of graphitization [46–49]. A slight shift was observed in the broad peaks of TC B10, TC C12, and TC D14 from 21.069^0, 20.933^0, and 20.698^0 respectively due to milled samples in HEBM. The diffraction patterns of AC were matched with the standard ICDD file (00-001-0646) confirming the formation of crystalline structures of the graphitic carbon. The obtained diffraction peaks are indexed to the corresponding peaks for the graphitic carbon (002), (100), and (101) crystal planes, which reflect the turbostratic carbon structure. Table 1 presents the angle 2θ (^{0}), d spacing (Å), intensity (cts), FWHM (2θ), and crystallite size (nm) of different samples. The crystallite size was measured by using the Scherrer equation (Eq. 1) calculated from the FWHM value of the high-intensity peak corresponding to (101) crystal plane of AC. The particle size is calculated by using Debye Scherrer's equation [50, 51],

$$D = 0.89\lambda / (\beta \cos\theta) \quad (1)$$

Where D is the crystallite size, λ is the wavelength of the X-ray used, θ is Bragg's angle and β is the full width half maximum.

Table 1

Angle 2θ (^{0}), d spacing (Å), intensity (cts), FWHM (2θ), and crystallite size (nm) of different samples from XRD spectra.

Sample	*2θ* /degree	d spacing/ Angstrom	Intensity/cts	FWHM (*2θ*)	Crystallite size (nm)
TC C12	35.5308	2.52457	129.27	0.5760	14.7
TC D14	44.4717	2.03557	97.25	0.7680	11.3
AC B10	44.5393	2.03263	304.90	0.1440	63.1
AC C12	44.5713	2.03125	261.80	0.2880	30.7
AC D14	44.6020	2.02992	1023.41	0.1920	46.7

The average crystallite size of AC for AC B10, AC C12, and AC D14 is less than 70 nm. The lowest crystallite size was obtained for AC C12 with an average size of 30.7 nm with a broad FWHM of 0.2880. It shows that the smaller the crystallite size, the greater the value of FWHM, with ‘displacement’ and ‘disordering’ as the main defects contributing to the broadening of diffraction peaks by increasing the milling time [52]. However, the FWHM displays a decrease to 0.1920 as the crystallite size slightly increased to 46.7 nm. Moreover, the intensity counts reflect the highest values for AC D14 with 1023.41 counts with the additional splitting of the highest peak. The peak splitting observed is due to the transition of carbon from a highly symmetric phase to a lower one. It also depicts the presence of a microporous wall structure of AC [53]. The XRD results confirmed that the synthesized AC has a better crystallographic structure and an organized aromatic carbon that is more stable than the amorphous carbon alone. Thus, these results were further discussed by Raman spectroscopic analysis.

The d-spacing values decreased as the milling time increased from TC C12 to TC D14. However, it slightly decreased in the range of ~ 2.03 for AC B10, AC C12, and AC D14. The value of d spacing is between 2.0 and 2.5 Å attributed to the distance between parallel planes of atoms that build the molecular nanostructures, thereby leading to intraparticle microporous nanostructures connected with various shapes and sizes [54].

Milling time affects the peak intensity which the peak intensity decreases as the milling time increases, and the peaks broaden disclosing size reduction that corresponds to the creation and accumulation of lattice defects. This event has been attributed to the deformation of powder particles from repeated fracturing, cold-welding, agglomeration, and deagglomeration [55]. Moreover, as the particle is reduced due to collision between balls, vial, and powder, the surface area to volume ratio is high, and tends to have a main peak at 2θ as can be observed for TC D14. Prolonged milling time can result in the ordering and crystallization of an amorphous matrix [38]. Besides, the peak indicating (002) becomes slightly sharper while the peak representing (100) becomes more intense. This shows that despite having a non-graphitized structure, carbon tends to crystallize.

Microstructural Analysis (FESEM)-EDX

EDX is an analytical method for determining the chemical and elemental composition of samples. Figure 4 presents the EDX findings for the elements in the AC. EDX revealed that carbon (C), oxygen (O), and potassium (K) were the most prevalent elements on the surface of all samples. The carbon element (C) is the most abundant element contained in each sample. Similar results were also found in previous studies of *Terminalia catappa* with carbon elements that varied from 69–75% [56]. Thus, the milled TC sample utilized for the preparation of activated carbon has the highest percentage of carbon elements between 93.22–93.77% compared to raw TC crush. Additionally, the sample contains oxygen (O) and potassium (K) amongst other elements. The O element is a result of the imperfect carbonization process and can also be caused by bonding during the activation process [57]. The K element may stem from a lack of thorough cleaning during the preparation process.

A morphology study of the activated carbon was performed by a field emission scanning electron microscopy (FESEM) analysis. Figure 5 (a) displays a raw TC sample image. Some studies have shown that the surface of TC is dense and rough [58]. The TC exhibited a very dense-like structure with the absence of pores (non-porous) and had no cavities as compared to other prepared ACs with average pores diameters of 62 nm. This was confirmed in a previous study where the surface porosity of the char products increased after the carbonization process, resulting in a large surface area with small voids on the surface [59]. The decreased density of AC formation results in a large surface area and the presence of rich mesoporous that results in potential lightweight electromagnetic wave-absorbing materials.

The ability of an adsorbent to perform adsorption depends greatly on its porosity and rougher surface morphology [60–63]. Thus, the surface morphology and porosity of the prepared ACs were tested by FESEM and the results are presented in Fig. 5(b-d). The findings suggest major fissures and channels of micro and mesoporous nature. The micrographs of the prepared ACs disclosed the porous structure progressively developing into a sponge-like structure as the particle size decreased. Irregular channels were also present in the sample at a high-milling time, which corresponds to a smaller particle size. The pores formation contributes to a better match between dielectric loss and magnetic loss, as well as the multiple reflections by the mesoporous structure [64–65]. Moreover, activating the sample with KOH resulted in samples b, c, and d containing open holes. According to some researchers, after the chemical activation process, KOH as the activating agent goes into the surface texture of the main material during the impregnation step and assists in developing a more porous structure [48, 66, 67]. Activated carbon with porous structure (irregular pores and broken edges) and the formation of cavities due to evaporation and gasification of activating agents were also observed by them [68, 69]. Consequently, it is anticipated that the activated carbon created using the KOH activation process will have a higher BET and micropore surface area [70–72].

RAMAN Structural Analysis

Figure 6 displays two significant peaks that were observed in all samples of TC powder and prepared ACs. These two peaks present the D-peak and G-peak observed at wavenumbers of 1342 cm^{-1} and 1582 cm^{-1}, respectively. The disordered and defective structures due to the vibration of sp^3 hybridized atoms

are represented by the D-band, whereas the graphitic structure of sp^2 bonded carbon atoms bonded in the hexagonal lattice is represented by the G-band [73, 74]. G-band also refers to the C-C bond stretching of all pairs of sp^2 atoms in both rings and chains attributed to E_2g_2 Raman active vibration mode [63, 75, 76]. The broad and strongly overlapping D (sp^3) and G (sp^2) bands at 1338 and 1583 cm^{-1} are similar to graphite, confirming the graphite-like structure of *Terminalia catappa* fruits. The dotted line indicates the shift of the D and G peaks to the lower wavenumber. The AC B10 exhibited sharper and higher D-band and G-band as compared to other AC samples. These higher peaks indicate the successful fabrication of the AC B10 as a carbon-based material with more crystalline structures as compared to others.

Table 2 shows the ratio of ID/IG for AC is nearly the same between 0.8 and 0.92 and is slightly lower than TC, demonstrating the higher amount of graphitic ordered carbon present due to double heating performed at high temperatures for carbonization and activation. The ID/IG ratio of ACs has been reported to range from 0.86 to 1.20 [77–79]. Although more CNSs are observed in SEM and TEM images, the ID/IG ratio displays a similar number of around 0.9, indicating similar graphitic structures are obtained with the formation of graphitized carbon (CNSs) and a smaller number of structural defects [80–82]. The ID/IG values suggested a defective structure or a lower graphitization degree in the resulting CNTs. According to Hussein et al. (2012), the ID/IG obtained in their research was 0.86 and 0.88, which was suggested as a defective structure or CNTs with lower graphitization [83]. Medhat et al. (2021) reported that the ratio of ID/IG is almost the same since an activating agent does not influence the structural shape of the activated carbon despite increasing the impregnation ratio of KOH [84]. The D-band of the three AC samples has approximately the same range of wavenumber from 1331.25 to 1341.61 cm^{-1}.

The width of the G peak can be used to determine the disordered samples as the higher disorder results in a higher width. The FWHM of the G-band shows the Raman shift to a lower number as the size of the particles of the ACs are reduced or increased milling time. FWHM displays a decrease in numbers from 61.93 to 29.13 as the size of particles is reduced. It also denotes that the percentage of defects appearing in the structure will be higher as the G-band is reduced since the broad peak of the G-band indicates a low graphitization of nano coils. This defect structure is preferable in this study as it contributes to a larger $S_{BET,}$ thus complementing the result of BET of AC B10 [73, 80, 81]. This correlates with the key factor for high adsorption capacity. The adsorbents with high defect structures demonstrated high SBET and more porous structures [85]. This characteristic is preferred as it assists to strengthen the binding interactions with the gas adsorbates [73, 86].

Table 2: Corresponding peak frequencies (Raman shift) for all TC and AC in Raman spectra.

Sample	D peak position (cm-1)	G peak position (cm-1)	Id/Ig ratio	FWHM-G	Sp2 cluster size/La
TC crush	1347.214	1588.935	1.014	61.934	48.876
AC B10	1341.610	1579.195	0.822	51.735	60.292
AC C12	1331.252	1577.533	0.920	45.969	53.870
AC D14	1335.812	1570.692	0.861	39.126	57.561

A pair of relatively broad G and D peaks can be classified by sp^2 clusters like α-Cs with bond angle disorder structure of activated carbon materials. The structure of α-Cs exhibits both crystallinity and amorphic since it is composed of a 3D network of nano graphite embedded in an amorphous background created by disordered carbon in the form of aliphatic chains. It is characterized by some cross-linkage structures present at the periphery of nano graphitic domains [87]. Moreover, the formation of G and D plots are overlapped or is close to those of G and D plots of α-Cs [88]. The part of the sp^2 cluster may link the winding short basal planes with bond angle order. In α-Cs, a few studies reported that sp^2-cluster size simply enhances the ID/IG ratio [89–91], thereby indicating the relative sp^2/sp^3 bonding ratio and the sp^2-cluster size. The sp^2-cluster size recorded the lowest TC crush, increasing to approximately 53 to 60 for AC B10, AC C12, and AC D14 probably because a smaller starting particle size creates or enlarges sp^2-cluster size. Some researchers reported that the size of AC affects the characteristics, and it can be optimized [92–93]. For example, the smallest AC particle in their research depicted higher specific surface area, pore volume, macropores, and fractions of sp^2-C and C = O, but lower ID/IG and fractions of sp^3-C and O-C = O compared to the largest AC particle.

The cluster size can also be associated with the band gap, thus, the larger the cluster size, the lower the band gap. Resultantly, the excitation energy is dominated by the resonantly enhanced peaks of sp^2 C clusters. The broad peaks thus provide detailed information on the bonding configuration of carbon atoms in grain boundaries as reported by [94].

Surface Area Analysis (BET)

The BET surface area (m^2/g) analysis method is the most common and extensively used method to calculate the surface area of different samples. Micromeritics ASAP 2020 instrument was used for the N_2 gas adsorption-desorption process at 77 K to determine the specific surface area and pore size distribution of different materials. Prior to analysis, the samples were degassed and heated at 110 ^oC for 12 hours. The nitrogen adsorption and desorption isotherms for all samples were measured. The BET equation involved is expressed as follows [95]:

1WP0P-1 = 1WmC + C-1WmC (PP0)

where: W = Weight of gas adsorbed, P/P_0 = Relative pressure, Wm = weight of adsorbate constituting a monolayer coverage, C = related to the energy of adsorption in the first adsorbed layer.

The S_{BET}, average pore diameter, and pore volume of ACs were measured by the nitrogen adsorption-desorption method, and the results are presented in Fig. 7. According to the IUPAC classification, the isotherm of all AC samples is type IV with an H4 type hysteresis loop [96, 97], presenting the predominance of mesopores between the carbon components or in the matrix, generating slit-shaped pores with a non-uniform size. Mesoporous materials with pore sizes between 50 nm and 2 nm are used to produce the type IV isotherm.

The hysteresis loop has also been presented in the isotherms at around $P/P0 = 0.4–1.0$ for all samples. The process of adsorption-desorption has capillary condensation due to the bimodal micro-mesoporous structure [84, 98]. The mesopores are filled at $P/P^o < 1$ due to the secondary process of capillary condensation, which is related to the hysteresis loop. Type H4 corresponds to limited amounts of mesopores limited by micropores and are given by many activated carbons and some other nanoporous adsorbents. These isotherms are composite. The initial phase of reversible micropore filling is followed by multilayer physisorption and capillary condensation in the simplest condition. One can frequently divide the isotherm into its component pieces by using an empirical method of analysis (such as the S-plot) [99, 100]. It, therefore, becomes apparent that on the comparatively small non-microporous portion of the adsorbent, the H4 loop is comparable to an H3 loop. The adsorptive ability, the most significant characteristic of activated carbon, correlated with the pore surface area. Generally, the adsorptive ability of activated carbon increases with increasing pore surface area. The BET surface area of the produced carbons is significantly influenced by the reaction conditions. By varying the carbonization and activation parameters, the pore structures of agricultural waste carbons can be modified to some extent. The result demonstrated that different milling time of starting powder affects the pore size distribution of ACs. Furthermore, the total pore volume and distribution of the volume of micropores, mesopores, and macropores slightly shifted by different milling times or particle sizes.

Table 3 summarizes the BET surface area (S_{BET}) and pore structure properties of the activated carbons with different parameters. The S_{BET} of AC B10, C12, and D14 are 1721.0050 m^2/g, 1617.4491 m^2/g, and 1241.5574 m^2/g, respectively, thereby reflecting that the milling time of the starting materials increase as the BET surface of the samples decreases. These findings can be explained by the destruction part of the internal porous structure of the material in the milling. The average pore diameter of the ACs depicts an increase in sizes, which are 3.5310 nm, 3.7418 nm, and 4.4876 nm, and the pore volume is 0.1401 cm^3/g, 0.1255 cm^3/g, and 0.1587 cm^3/g respectively. According to Ding et al. (2021), the adsorbent diameter was defined by IUPAC as mesopore if its within 2 and 50 nm, micropore if its < 2 nm, and macropore if its > 50 nm [101]. Based on these results, the samples are considered mainly mesoporous.

Table 3
BET surface area (S_{BET}) and pore structure properties of the activated carbons with different parameters

Sample	BET surface area, S_{BET} (m^2/g)	Average pore size (nm)	Pore volume (cm^3/g)
AC B10	1721.0050	3.5310	0.1401
AC C12	1617.4491	3.7418	0.1255
AC D14	1241.5574	4.4876	0.1587

Hevira et al. (2021) reported that the specific surface area of the TC shell was 69.88 m^2/g before biosorption and 51.52 m^2/g after biosorption of MB [102]. On the other hand, the specific surface area of activated carbon with a pre-carbonization time of 2 h and 3 h are 279 and 303 m^2/g, respectively [103]. Thus, the specific surface area increased ~6 times (from 279 to 1721.0050 m^2/g) as the particle size was reduced, indicating the higher sensitivity of the surface area to size reduction as reported by Rahman et al. (2009) [104]. Hence, smaller particle size makes the smaller nanoparticles suitable for the applications, such as fillers in advanced nanocomposites and as a catalyst [105].

Conclusion

This study successfully synthesized activated carbon-based *Terminalia catappa* fruit waste at different starting particle sizes. Nanometer starting particle size in synthesizing activated carbon produced a higher percentage yield of AC and the carbon percentages were maintained until 93% of carbon content. Increasing the milling time of smaller crystallite size results in a greater value of FWHM, 'displacement', and 'disordering' defects, which contribute to the broadening of diffraction peaks. The peaks broadening depicting size reduction also corresponds to the creation and accumulation of lattice defects. The micrographs of the prepared ACs also demonstrate the porous structure progressively developing into a sponge-like structure as the particle size decreased. Irregular channels were also present in the sample at high milling time, which corresponds to a smaller particle size. As the milling time of the starting materials increase, the BET surface of the samples decreases. These findings can be explained by the destruction part of the internal porous structure of the material in the milling. Moreover, the specific surface area increased ~6 times (from 279 to 1721.0050 m^2/g) as the particle size was reduced, indicating that the surface area is more sensitive to size reduction. Thus, this study revealed that the milling time for starting particle size of *Terminalia catappa* fruit waste to synthesize activated carbon does affect the properties of AC, carbon content, morphology, pore diameter, and surface area BET.

Declarations

Acknowledgements

The research was supported by University Research Grant (USIM-RACER Grant) (PPPI/USIM-RACER_0120/KGI/051000/11920) and Ministry of Education Malaysia through Fundamental Research Grant Scheme (FRGS/1/2020/STG05/USIM/02/3) (USIM/FRGS/KGI/KPT/52020). The authors also express deepest gratitude and pleasure towards Institute of Nanoscience and Nanotechnology (ION2, UPM), Faculty of Science and Technology USIM, Kolej GENIUS Insan, i-CRIM Centralized Lab, Centre for Research and Instrumentation Management (CRIM) UKM and Chemistry Lab, Department of Chemical Sciences, Faculty of Science and Technology UKM for providing the apparatus and equipment used in the laboratory.

Competing interests: Authors declare that there is no competing interests.

Authors' contributions:

Writing-original draft preparation: Noorain Purhanudin, Fadzidah Mohd Idris, Nur Fadilah Paharuddin Pallan

Conceptualization and Methodology: Noorain Purhanudin, Fadzidah Mohd Idris

Writing-review and editing: Noorain Purhanudin, Fadzidah Mohd Idris

Funding acquisition: Fadzidah Mohd Idris

Funding:

University Research Grant (USIM-RACER Grant) (PPPI/USIM-RACER_0120/KGI/051000/11920) and Ministry of Education Malaysia through Fundamental Research Grant Scheme (FRGS/1/2020/STG05/USIM/02/3) (USIM/FRGS/KGI/KPT/52020)

References

1. Y. Chen, Y. Zhu, Z. Wang, Y. Li, L. Wang, L. Ding, X. Gao, Y. Ma, and Y. Guo, Adv Colloid Interface Sci **163**, 39 (2011).
2. M.S. Reza, C.S. Yun, S. Afroze, N. Radenahmad, M.S.A. Bakar, R. Saidur, J. Taweekun, and A.K. Azad, Arab J Basic Appl Sci **27**, 208 (2020).
3. W. Li, Q. Zhang, J. Zhang, Y. Zheng, H. Zhang, J. Liu, and Y. Cui, J Mater Sci **56**, 19969 (2021).
4. A.N. Yusoff, M.H. Abdullah, S.H. Ahmad, S.F. Jusoh, A.A. Mansor, and S.A.A. Hamid, J Appl Phys **92**, 876 (2002).
5. R.H. Hesas, W.M.A.W. Daud, J.N. Sahu, and A. Arami-Niya, J Anal Appl Pyrolysis **100**, 1 (2013).
6. A.A. Abd, M.R. Othman, and J. Kim, Environmental Science and Pollution Research **28**, 43329 (2021).
7. W.K. Koo, M.A. Sulaiman, N.S. Subki, M. Mohamed, M.N. Masri, M.B. Abu Bakar, M.H. Mohamad Amini, and N.A.A. Nik Yusuf, in *Materials Science Forum* (Trans Tech Publ, 2016), pp. 432–437.

8. X.-L. Su, J.-R. Chen, G.-P. Zheng, J.-H. Yang, X.-X. Guan, P. Liu, and X.-C. Zheng, Appl Surf Sci **436**, 327 (2018).
9. J. Mohammed, N.S. Nasri, M.A.A. Zaini, U.D. Hamza, and F.N. Ani, Int Biodeterior Biodegradation **102**, 245 (2015).
10. W. Ao, J. Fu, X. Mao, Q. Kang, C. Ran, Y. Liu, H. Zhang, Z. Gao, J. Li, and G. Liu, Renewable and Sustainable Energy Reviews **92**, 958 (2018).
11. P. González-García, Renewable and Sustainable Energy Reviews **82**, 1393 (2018).
12. R. Panwar, S. Puthucheri, D. Singh, V. Agarwala, and J.-R. Lee, Advanced Composite Materials **26**, 99 (2017).
13. A.M. Abioye and F.N. Ani, J Teknol **79**, (2017).
14. Y. Fu, Y. Shen, Z. Zhang, X. Ge, and M. Chen, Science of the Total Environment **646**, 1567 (2019).
15. Z. Xu, M. He, X. Xu, X. Cao, and D.C.W. Tsang, Bioresour Technol **338**, 125555 (2021).
16. W. Li, L. Zhang, J. Peng, N. Li, and X. Zhu, Ind Crops Prod **27**, 341 (2008).
17. C.A. Toles, W.E. Marshall, M.M. Johns, L.H. Wartelle, and A. McAloon, Bioresour Technol **71**, 87 (2000).
18. N.F. Jariah, M.A. Hassan, Y.H. Taufiq-Yap, and A.M. Roslan, Processes **9**, 1198 (2021).
19. A.G. Georgiadis, N.D. Charisiou, and M.A. Goula, Catalysts **10**, 521 (2020).
20. A. Tomczyk, Z. Sokołowska, and P. Boguta, Rev Environ Sci Biotechnol **19**, 191 (2020).
21. H. Sayğılı and F. Güzel, J Clean Prod **113**, 995 (2016).
22. M.A. Bedmohata, A.R. Chaudhari, S.P. Singh, and M.D. Choudhary, International Journal of Advanced Research in Chemical Science (IJARCS) **2**, 1 (2015).
23. J.O. Ighalo, D.V. Onifade, and A.G. Adeniyi, International Journal of Sustainable Engineering **14**, 1059 (2021).
24. K.R. Thines, E.C. Abdullah, N.M. Mubarak, and M. Ruthiraan, Renewable and Sustainable Energy Reviews **67**, 257 (2017).
25. A.H. Restrepo, J.M. Ríos, F. Arango, E. Correa, A.A. Zuleta, A. Valencia-Escobar, F.J. Bolivar, J.G. Castaño, and F.E. Echeverría, The International Journal of Advanced Manufacturing Technology **110**, 1681 (2020).
26. Y. Zhang, Q. Wang, and C.S. Ramachandran, Diam Relat Mater **104**, 107748 (2020).
27. M. Calero, A. Pérez, G. Blázquez, A. Ronda, and M.A. Martín-Lara, Ecol Eng **58**, 344 (2013).
28. J.S. Benjamin, Metallurgical Transactions **1**, 2943 (1970).
29. A. Rittidech and P. Khotsongkram, Am J Appl Sci **3**, 1760 (2006).
30. A. Manikandan, K.S. Subramanian, and K. Pandian, Magnesium **3**, 0 (2013).
31. N.S. Nasri, J. Mohammed, M.A. Ahmad Zaini, U.D. Hamza, and F.N. Ani, in *Adv Mat Res* (Trans Tech Publ, 2014), pp. 219–223.
32. S.T. Dhaarini, R. Gomathi, C.M. Kumaar, and K. Yogeswari, Mater Today Proc **45**, 6016 (2021).

33. S. Vitolo and M. Seggiani, Geothermics **31**, 431 (2002).
34. A. Shepherd, 13th Annual EnviroExpo, Boston, Massachusetts (May 2001, 4 Pages) (2001).
35. E. Misran, M. Sarah, Irvan, S.F. Dina, S.A.A. Harahap, and A. Nazar, J Phys Conf Ser **1542**, (2020).
36. L.G. Hassan, A. Uba, S.W. Hassan, S. Yusuf, M.A. Sokoto, and A.N. Itodo, Journal of Energy and Environmental Sustainability **6**, 36 (2018).
37. N.S. Sulaiman, R. Hashim, M.H.M. Amini, M. Danish, and O. Sulaiman, J Clean Prod **198**, 1422 (2018).
38. A. Hajalilou, A. Kianvash, H. Lavvafi, and K. Shameli, Journal of Materials Science: Materials in Electronics **29**, 1690 (2018).
39. A.V. Rane, K. Kanny, V.K. Abitha, and S. Thomas, in *Synthesis of Inorganic Nanomaterials* (Elsevier, 2018), pp. 121–139.
40. C. Weidenthaler and M. Felderhoff, Energy Environ Sci **4**, 2495 (2011).
41. S.C. Zhang, W.G. Fahrenholtz, G.E. Hilmas, and E.J. Yadlowsky, J Eur Ceram Soc **30**, 1373 (2010).
42. Á. Kukovecz, T. Kanyó, Z. Kónya, and I. Kiricsi, Carbon N Y **43**, 994 (2005).
43. H. Abdullah and H. Wu, Energy & Fuels **23**, 4174 (2009).
44. A. Macías-García, D. Torrejón-Martín, M.Á. Díaz-Díez, and J.P. Carrasco-Amador, J Energy Storage **25**, 100829 (2019).
45. J. Bedia, M. Peñas-Garzón, A. Gómez-Avilés, J.J. Rodriguez, and C. Belver, C (Basel) **6**, 21 (2020).
46. E. Elaiyappillai, R. Srinivasan, Y. Johnbosco, P. Devakumar, K. Murugesan, K. Kesavan, and P.M. Johnson, Appl Surf Sci **486**, 527 (2019).
47. E. Elanthamilan, B. Sriram, S. Rajkumar, C. Dhaneshwaran, N. Nagaraj, J.P. Merlin, A. Vijayan, and S.-F. Wang, Mater Res Bull **112**, 390 (2019).
48. Z. Xie, J. Yang, X. Huang, and Y. Huang, J Eur Ceram Soc **19**, 381 (1999).
49. Y. Ji, T. Li, L. Zhu, X. Wang, and Q. Lin, Appl Surf Sci **254**, 506 (2007).
50. S. Mustapha, J.O. Tijani, M.M. Ndamitso, A.S. Abdulkareem, D.T. Shuaib, A.T. Amigun, and H.L. Abubakar, Int Nano Lett **11**, 241 (2021).
51. T. Amutha, M. Rameshbabu, S. Muthupandi, and K. Prabha, Mater Today Proc **49**, 2624 (2022).
52. Y. Wang, Y. Tian, Y. Wang, H. Geng, and Z. Zhang, Intermetallics (Barking) **16**, 121 (2008).
53. N.K. Kalagatur, K. Karthick, J.A. Allen, O.S. Nirmal Ghosh, S. Chandranayaka, V.K. Gupta, K. Krishna, and V. Mudili, Front Pharmacol **8**, 760 (2017).
54. P.J. Wibawa, M. Nur, M. Asy'ari, and H. Nur, Heliyon **6**, e03546 (2020).
55. A. Hajalilou, M. Hashim, M. Nahavandi, and I. Ismail, Advanced Powder Technology **25**, 423 (2014).
56. E. Taer, A. Afrianda, R. Taslim, A. Agustino, A. Apriwandi, and U. Malik, in *J Phys Conf Ser* (IOP Publishing, 2018), p. 12007.
57. S.A. and C.J. Jankowski H, *Activ. Carbon First Ed.* ((Ellis Horwood, London), 1991).

58. N. Mehmandost, N. Goudarzi, M. Arab Chamjangali, and G. Bagherian, Journal of the Iranian Chemical Society **19**, 3769 (2022).
59. M.S. Shamsuddin, N.R.N. Yusoff, and M.A. Sulaiman, Procedia Chem **19**, 558 (2016).
60. M. Yaseen, S. Ullah, W. Ahmad, S. Subhan, and F. Subhan, Fuel **284**, 119102 (2021).
61. M. Arami, N.Y. Limaee, N.M. Mahmoodi, and N.S. Tabrizi, J Hazard Mater **135**, 171 (2006).
62. C. Song, Catal Today **86**, 211 (2003).
63. H. Xu, X. Yin, M. Zhu, M. Han, Z. Hou, X. Li, L. Zhang, and L. Cheng, ACS Appl Mater Interfaces **9**, 6332 (2017).
64. J. Zhou, J. He, G. Li, T. Wang, D. Sun, X. Ding, J. Zhao, and S. Wu, The Journal of Physical Chemistry C **114**, 7611 (2010).
65. Y. Du, T. Liu, B. Yu, H. Gao, P. Xu, J. Wang, X. Wang, and X. Han, Mater Chem Phys **135**, 884 (2012).
66. S.-C. Hu, J. Cheng, W.-P. Wang, G.-T. Sun, L.-L. Hu, M.-Q. Zhu, and X.-H. Huang, Renew Energy **177**, 82 (2021).
67. M.O. Prakash, G. Raghavendra, S. Ojha, and M. Panchal, Mater Today Proc **39**, 1476 (2021).
68. S.K. Thakur, T.S. Kong, and M. Gupta, Materials Science and Engineering: A **452**, 61 (2007).
69. D.A. Jones, T.P. Lelyveld, S.D. Mavrofidis, S.W. Kingman, and N.J. Miles, Resour Conserv Recycl **34**, 75 (2002).
70. J. Guo and A.C. Lua, Microporous and Mesoporous Materials **32**, 111 (1999).
71. Y. Sun and P.A. Webley, Chemical Engineering Journal **162**, 883 (2010).
72. M. Song, B. Jin, R. Xiao, L. Yang, Y. Wu, Z. Zhong, and Y. Huang, Biomass Bioenergy **48**, 250 (2013).
73. F.E.C. Othman, N. Yusof, S. Samitsu, N. Abdullah, M.F. Hamid, K. Nagai, M.N.Z. Abidin, M.A. Azali, A.F. Ismail, and J. Jaafar, Journal of CO2 Utilization **45**, 101434 (2021).
74. S. Goel, A. Garg, H.B. Baskey, M.K. Pandey, and S. Tyagi, J Alloys Compd **875**, 160028 (2021).
75. S. Wee, "Spectro-Electrochemical Study of Staging in Graphitic Electrodes for Aluminum Batteries." PhD diss., 2019.
76. A.S. Pannu, "Synthesis of 2D nanomaterial and their application in opto-electronic devices and sensing." PhD diss., Queensland University of Technology, 2021.
77. I. Abdalla, J. Shen, J. Yu, Z. Li, and B. Ding, Sci Rep **8**, 1 (2018).
78. L.L. Adebayo, H. Soleimani, N. Yahya, Z. Abbas, A.T. Ridwan, and F.A. Wahaab, Applied Sciences **9**, 3877 (2019).
79. F.A. Wahaab, L.L. Adebayo, A.A. Adekoya, I.G. Hakeem, B. Alqasem, and A.M. Obalalu, J Alloys Compd **836**, 155272 (2020).
80. D. Boufades, S.H. Née Mesdour, A. Moussiden, H. Benmebrouka, C. Hérold, and O. Kaddour, Fullerenes, Nanotubes and Carbon Nanostructures **28**, 716 (2020).
81. H. Kristianto, A.A. Arie, R.F. Susanti, M. Halim, and J.K. Lee, in *IOP Conf Ser Mater Sci Eng* (IOP Publishing, 2016), p. 12034.

82. F. Qin and C. Brosseau, J Appl Phys **111**, 4 (2012).
83. M.Z. Hussein, S.A. Zakarya, S.H. Sarijo, and Z. Zainal, J Nanomater **2012**, (2012).
84. A. Medhat, H.H. El-Maghrabi, A. Abdelghany, N.M.A. Menem, P. Raynaud, Y.M. Moustafa, M.A. Elsayed, and A.A. Nada, Applied Surface Science Advances **3**, 100037 (2021).
85. Y. Liu and J. Wilcox, Environ Sci Technol **45**, 809 (2011).
86. J. Hayashi, T. Horikawa, I. Takeda, K. Muroyama, and F.N. Ani, Carbon N Y **40**, 2381 (2002).
87. P. Sharma, G. Sharma, and R. Punia, Applied Physics A **127**, 1 (2021).
88. N. Shimodaira and A. Masui, J Appl Phys **92**, 902 (2002).
89. R.O. Dillon, J.A. Woollam, and V. Katkanant, Phys Rev B **29**, 3482 (1984).
90. N.H. Cho, K.M. Krishnan, D.K. Veirs, M.D. Rubin, C.B. Hopper, B. Bhushan, and D.B. Bogy, J Mater Res **5**, 2543 (1990).
91. J.W. Ager, IEEE Trans Magn **29**, 259 (1993).
92. D.G. Kim and S.O. Ko, J Environ Chem Eng **10**, 107179 (2022).
93. N. Bolan, S.A. Hoang, J. Beiyuan, S. Gupta, D. Hou, A. Karakoti, S. Joseph, S. Jung, K.-H. Kim, and M.B. Kirkham, International Materials Reviews **67**, 150 (2022).
94. M. Veres, M. Koós, S. Tóth, and L. Himics, in *IOP Conf Ser Mater Sci Eng* (IOP Publishing, 2010), p. 12023.
95. M.A. El-Bindary, I.M. El-Deen, and A.F. Shoair, J. Mater. Environ. Sci **10**, 604 (2019).
96. K.S.W. Sing, Pure and Applied Chemistry **57**, 603 (1985).
97. A. Boruah, A. Rasheed, V.A. Mendhe, and S. Ganapathi, J Pet Explor Prod Technol **9**, 1041 (2019).
98. T.B. Gebreegziabher, S. Wang, and H. Nam, J Environ Chem Eng **7**, 103234 (2019).
99. S.J. Gregg, K.S.W. Sing, and H.W. Salzberg, J Electrochem Soc **114**, 279Ca (1967).
100. K.S.W. Sing and R.T. Williams, Adsorption Science & Technology **22**, 773 (2004).
101. C. Ding, J. He, H. Wu, and X. Zhang, Minerals **11**, 298 (2021).
102. L. Hevira, J.O. Ighalo, H. Aziz, and R. Zein, Journal of Industrial and Engineering Chemistry **97**, 188 (2021).
103. A. Maryani, R. Farma, and M. Deraman, Applied Science and Technology **1**, 204 (2017).
104. I.A. Rahman, P. Vejayakumaran, C.S. Sipaut, J. Ismail, and C.K. Chee, Mater Chem Phys **114**, 328 (2009).
105. K.J. Klabunde and R.M. Richards, Nanoscale Materials in Chemistry (John Wiley & Sons 2009).

Figures

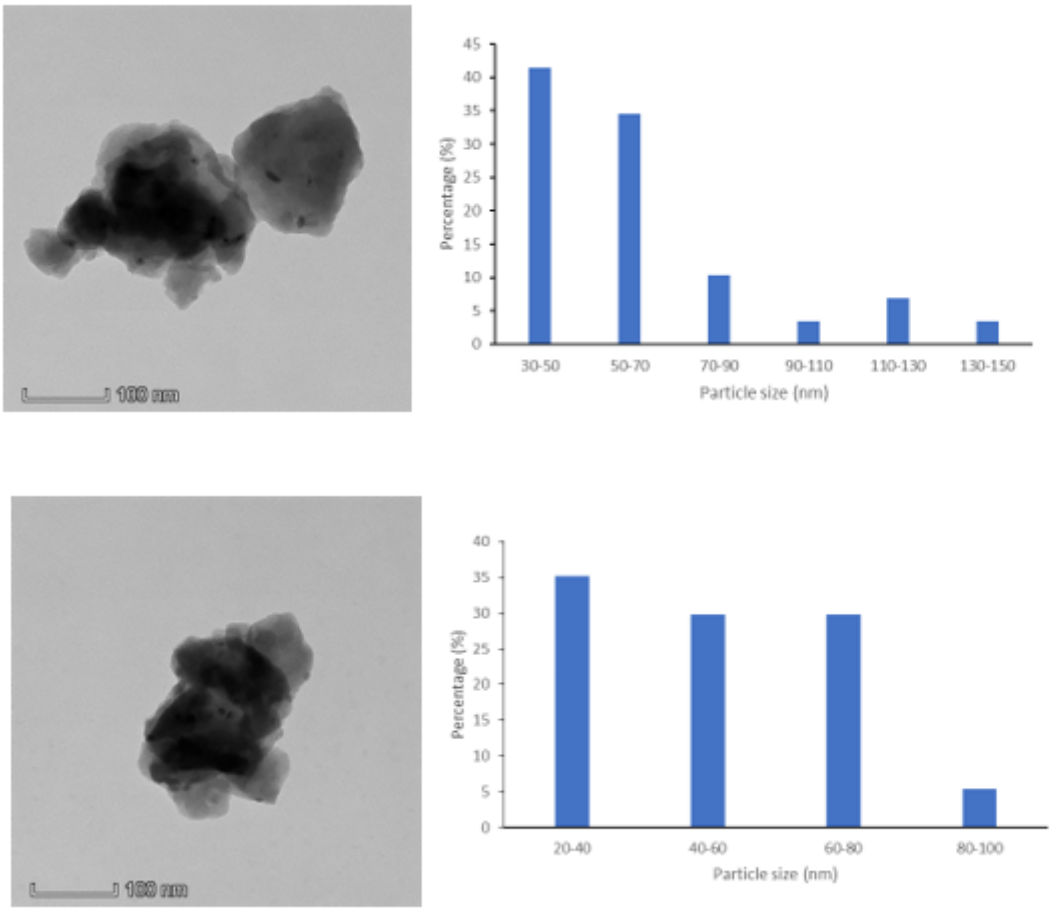

Figure 1

TEM micrograph and particle size distribution of TC A0 (a,b) and TC C12 (c,d).

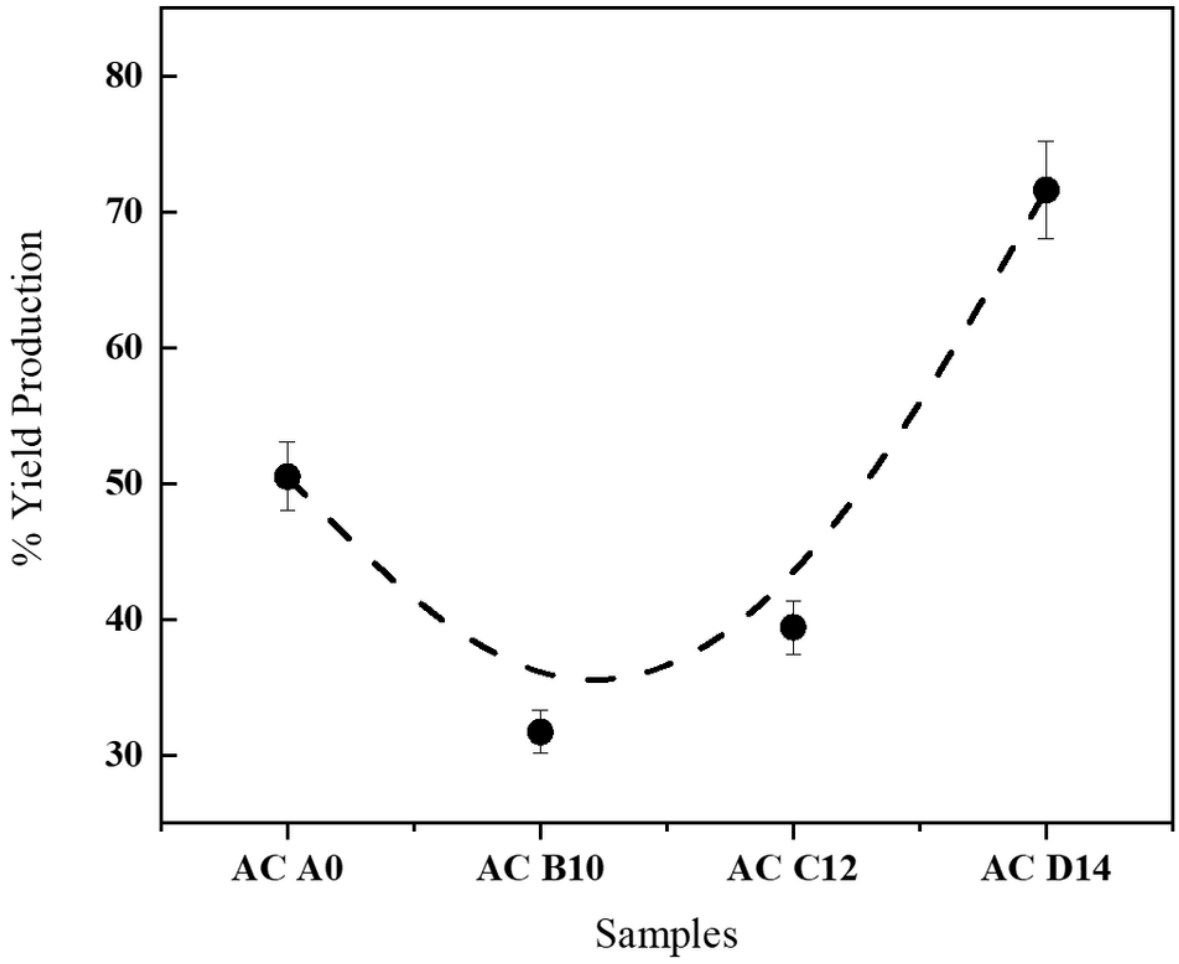

Figure 2

Percentage yield of activated carbon with different samples.

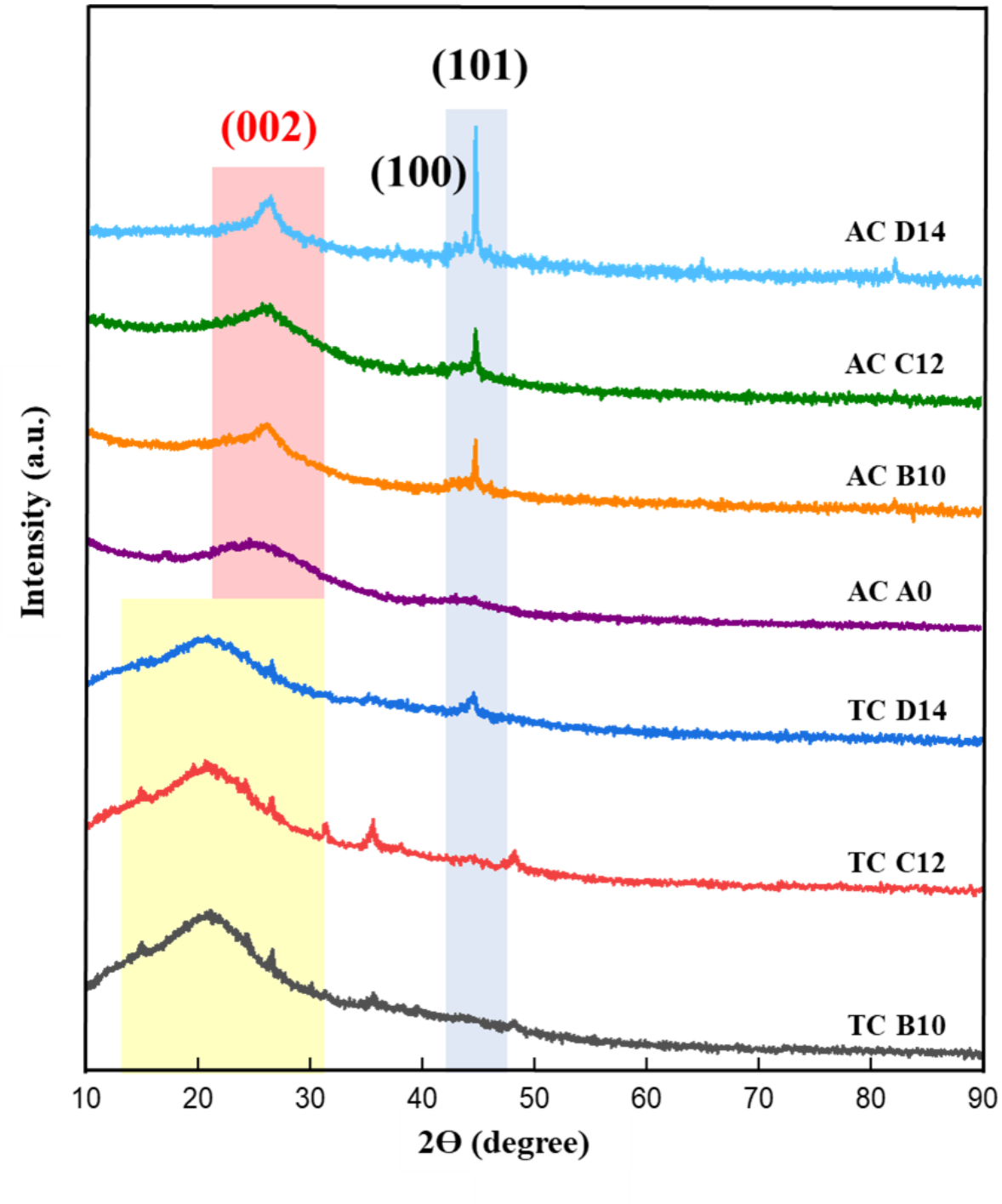

Figure 3

X-ray diffraction of milled *Terminalia catappa* (TC) and activated carbon (AC) from *Terminalia catappa*powder.

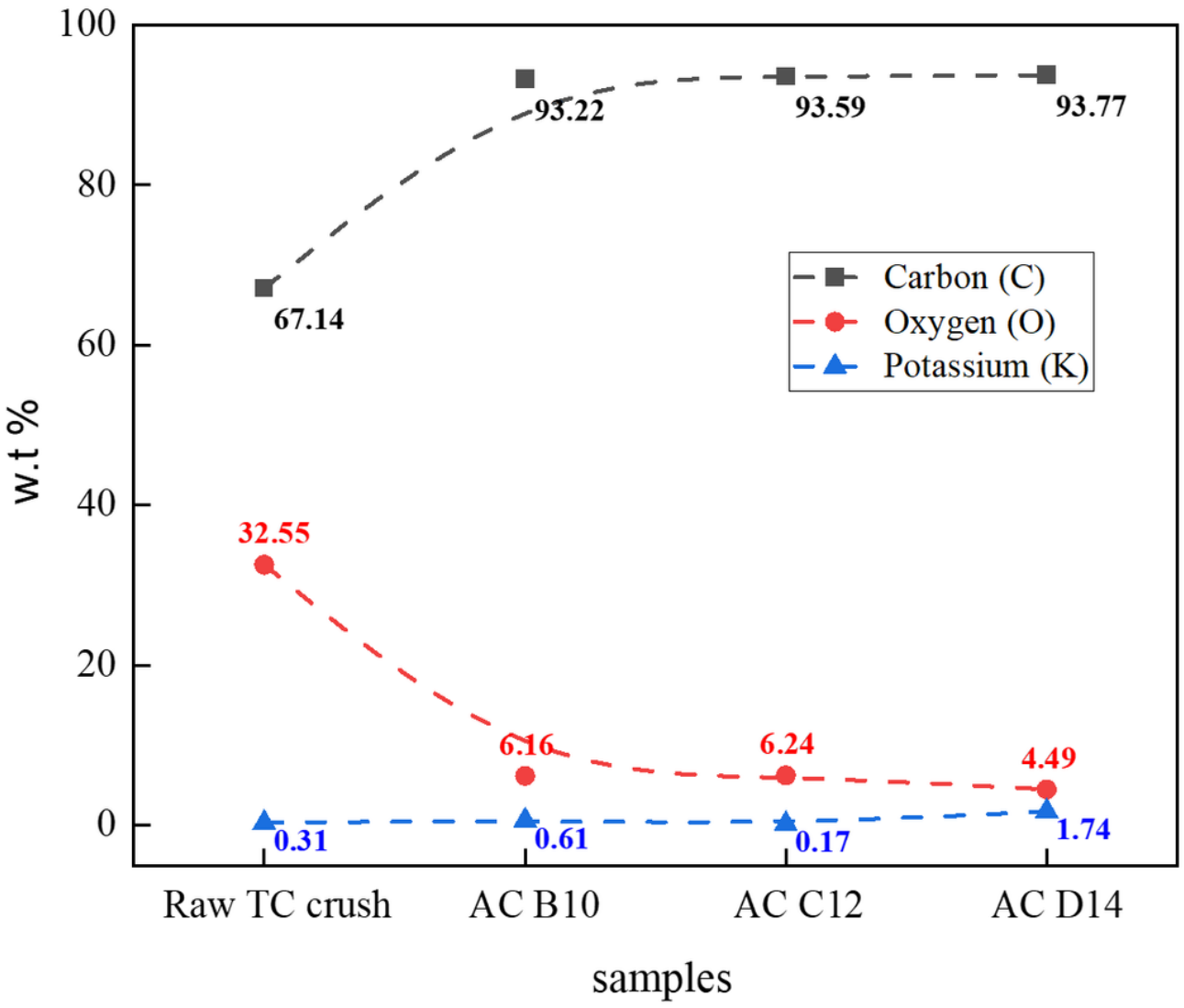

Figure 4

Percentages of elements in raw TC crush, AC B10, AC C12, and AC D14.

- - - The dotted lines refer to the guidelines.

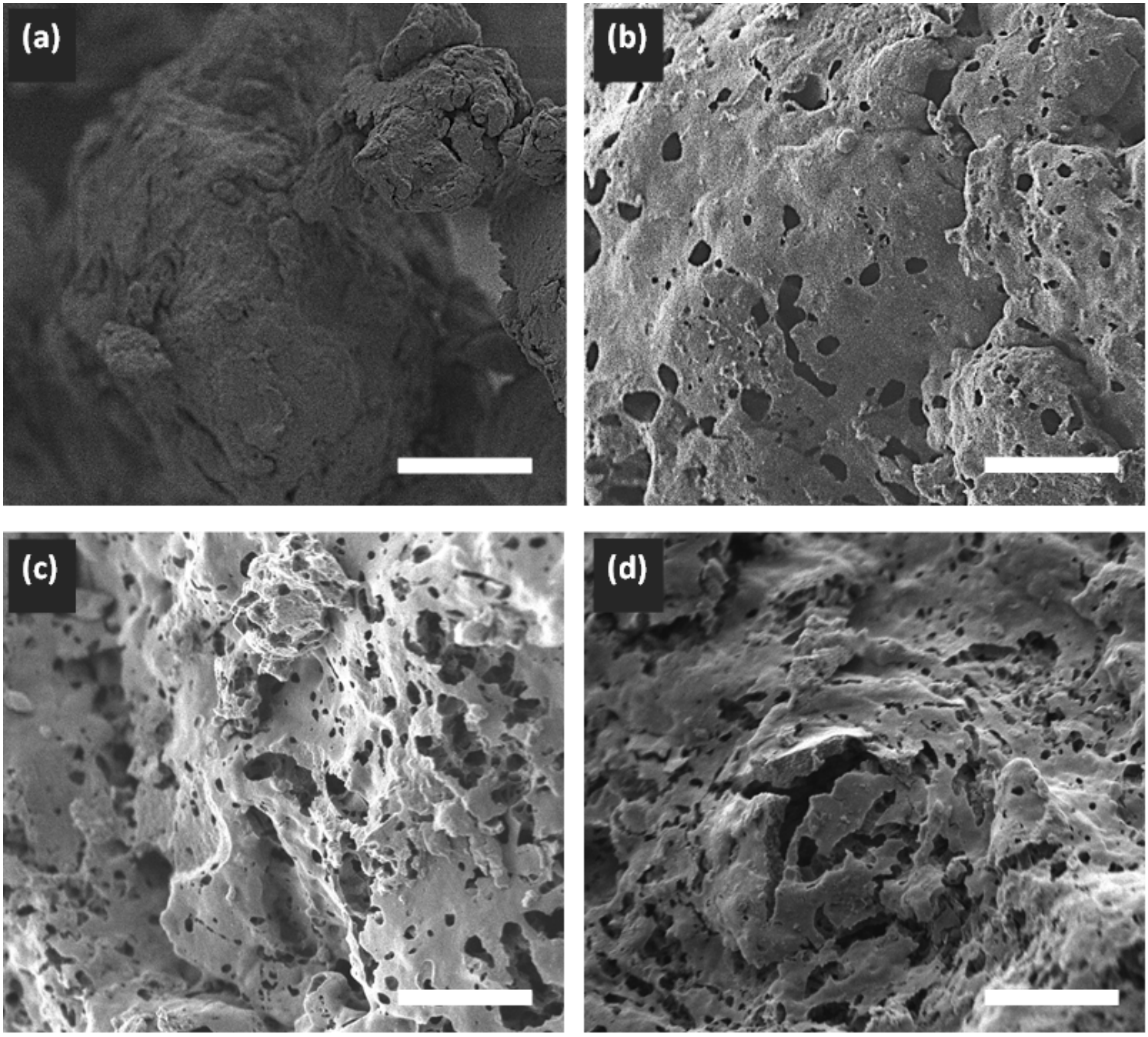

Figure 5

FESEM images of (a) TC crush, (b) AC 10, (c) AC 12, and (d) AC D14 at different milling times of 10 hours, 12 hours, and 14 hours, respectively.

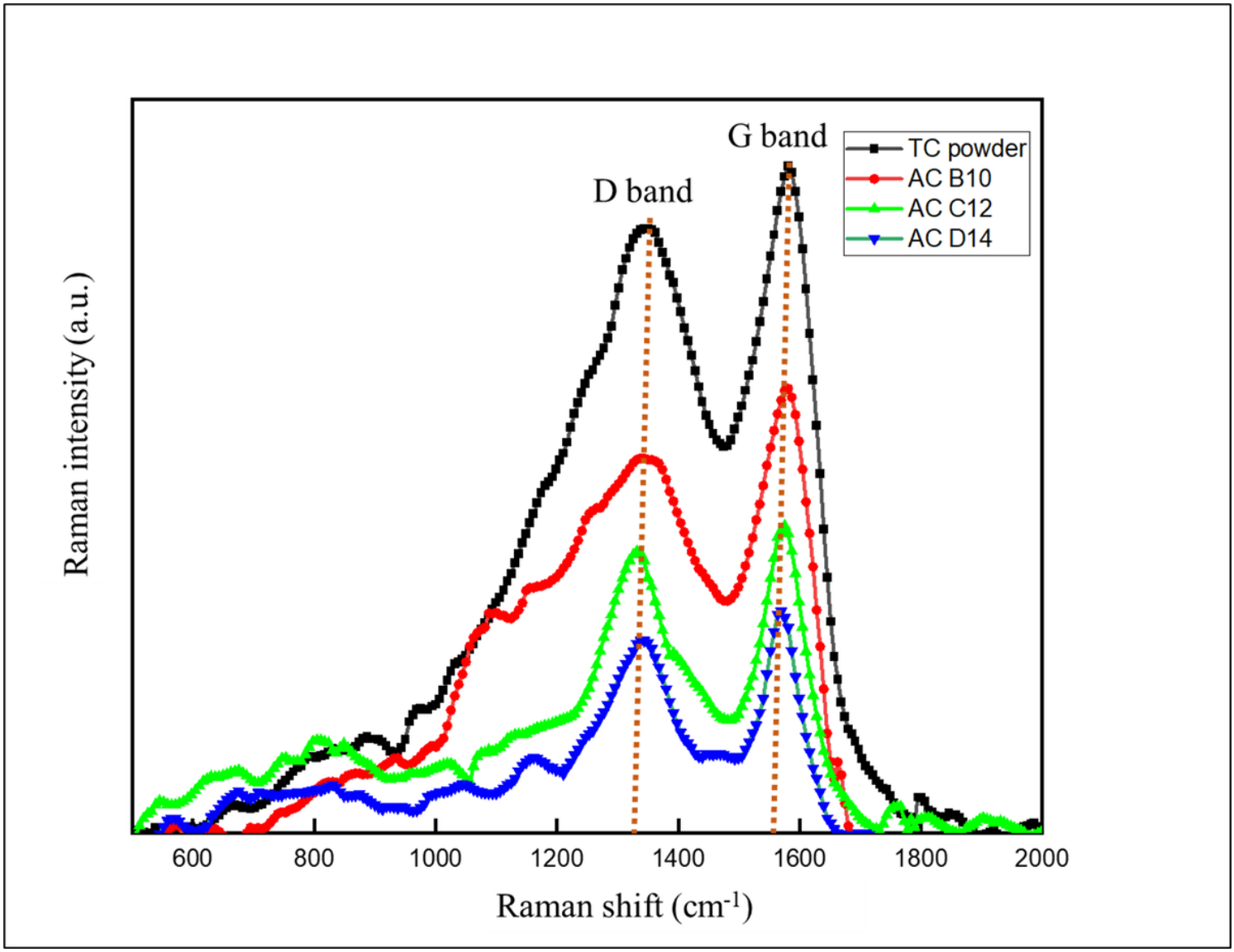

Figure 6

Raman spectrum of agricultural waste-derived activated carbon.

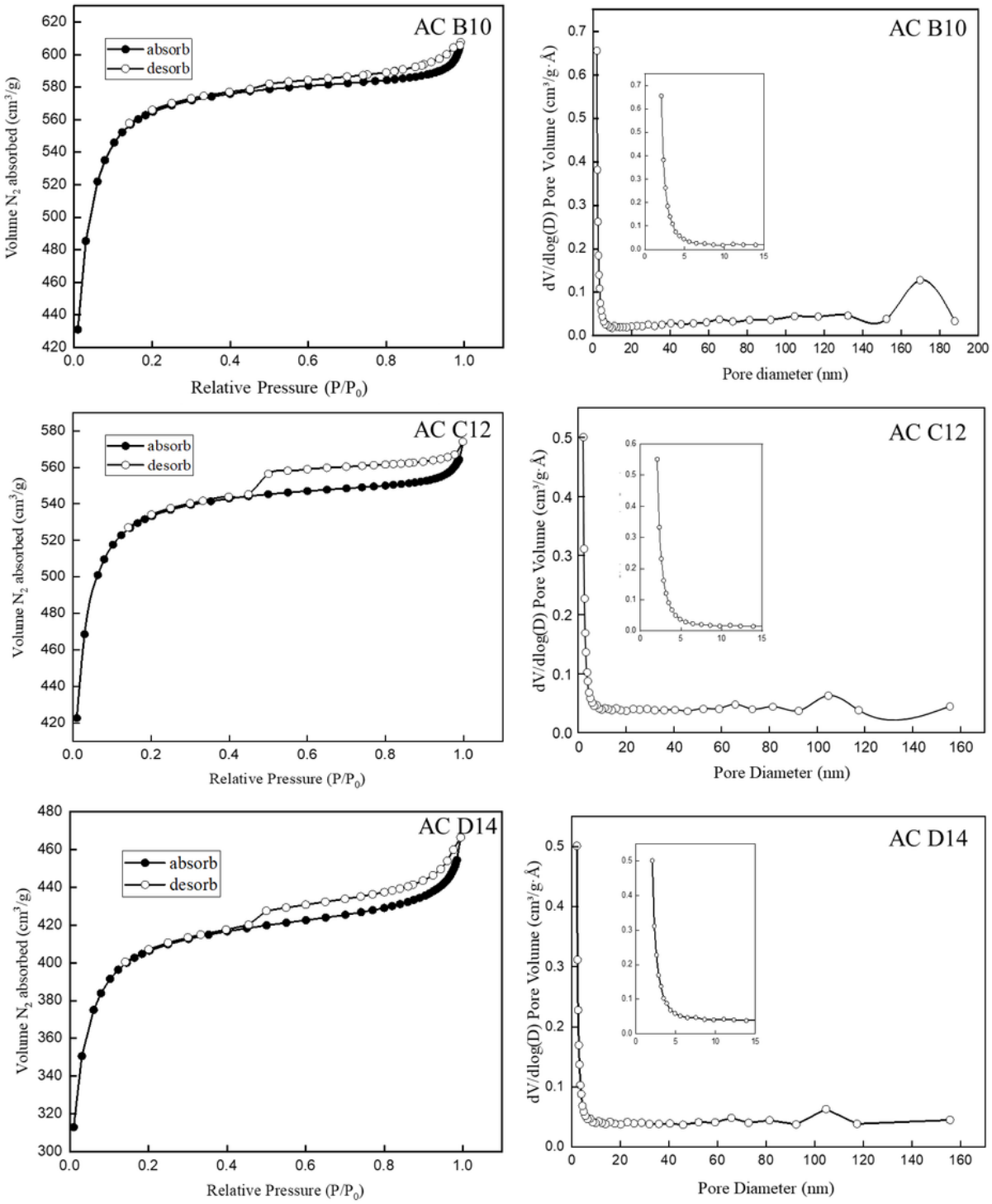

Figure 7

Adsorption isotherms of N2 at 77K for AC B10, AC B12, and AC D14.

Supplementary Files

This is a list of supplementary files associated with this preprint. Click to download.

- GraphicalAbstract.png